

Fabrication of FeF₃ nanocrystals dispersed into a porous carbon matrix as a high performance cathode material for lithium ion batteries

Cite this: *J. Mater. Chem. A*, 2013, **1**, 15060

Ruguang Ma,^{ab} Man Wang,^b Pengpeng Tao,^a Yu Wang,^b Chenwei Cao,^b Guangcun Shan,^b Shiliu Yang,^b Liujiang Xi,^b Jonathan C. Y. Chung^b and Zhouguang Lu^{*a}

FeF₃/C nanocomposites, where FeF₃ nanocrystals had been dispersed into a porous carbon matrix, were successfully fabricated by a novel vapour–solid method in a tailored autoclave. Phase evolution of the reaction between the precursor and HF solution vapour under air and argon gas atmospheres were investigated. The results showed that the air in the autoclave played an important role in driving the reaction to form FeF₃. The as-prepared FeF₃/C delivered 134.3, 103.2 and 71.0 mA h g^{−1} of charge capacity at a current density of 104, 520, and 1040 mA g^{−1} in turn, exhibiting superior rate capability to the bare FeF₃. Moreover, it displayed stable cycling performance, with a charge capacity of 196.3 mA h g^{−1} at 20.8 mA g^{−1}. EIS and BET investigations indicated that the good electrochemical performance can be attributed to the good electrical conductivity and high specific surface area that result from the porous carbon matrix.

Received 6th August 2013

Accepted 30th September 2013

DOI: 10.1039/c3ta13086j

www.rsc.org/MaterialsA

1. Introduction

Nowadays, lithium ion batteries (LIBs) play an incomparable role in powering portable electronic devices, such as laptop/tablet computers, cell phones and digital cameras.¹ However, their potential application in large-scale energy storage systems (*e.g.* electric vehicles) is still an attractive challenge due to the lack of advanced electrode materials, especially cathode materials with higher specific energy/power density. Therefore, extensive efforts have been made to explore facile and productive methods of fabricating cathode materials and to identify the effects of different factors on the electrochemical performance of the as-obtained materials.^{2–5} The capacity of classical cathode materials based on Li intercalation/deintercalation reactions is inherently limited by the mechanism of one-electron redox chemistry (1 e[−] per formula unit).⁶ Even when this kind of material is fully developed, its capacity is still not high enough to satisfy the requirements of the transport market.⁷ In contrast, conversion reaction compounds, such as MF_x (M: Fe, Mn, Co, Cu, Ni), possess the advantage of the ability to transfer multi-electrons per formula unit, thereby exhibit high theoretical specific capacity. Among them, iron trifluoride (FeF₃) has attracted considerable interest as one of the most promising

cathode materials because of its high theoretical specific capacity of 712 mA h g^{−1} and good thermal stability.^{8a}

However, low electronic conductivity and sluggish kinetics are fatal obstacles to the commercial application of FeF₃ as a high-capacity cathode material in LIBs. To overcome these drawbacks, one strategy is to fabricate FeF₃-based nanocomposites, by which the downsizing of the FeF₃ particles substantially accelerates the reaction rate of lithiation and delithiation and simultaneously the coupling of FeF₃ nanoparticles with highly conductive carbon considerably improves the rate capability of the FeF₃ active materials.^{8b} For example, in 2003, FeF₃/C nanocomposites were fabricated by Amatucci's group *via* a high-energy mechanical milling method, which exhibited high capacity but low cyclability at 7.58 mA g^{−1}, demonstrating the potential of FeF₃ to be used as a cathode material.^{9,10} The addition of MoS₂ into FeF₃ *via* ball-milling was investigated by the Wang group and found to be helpful for improving the electrochemical performance.¹¹ Li *et al.* synthesized carbon nanotube-wired iron fluorides (FeF_{2.5}·0.5H₂O and FeF₃·0.33H₂O) by utilizing an ionic liquid as the raw material to deliver and improve capacity and rate performances compared to counterparts without carbon nanotubes.² Kang's group reported the fabrication of FeF₃ nanoflowers on the carbon nanotubes with a high capacity of 210 mA h g^{−1} over 30 cycles at 20 mA g^{−1}.^{12a} Yang's group investigated the effect of *in situ* Fe₂O₃ coating on the electrochemical performance of FeF₃, pointing out that even a small amount of Fe₂O₃ has a great influence on the improvement of electrochemical performance, although the improvement is inferior to that obtained by mixing with carbon-based conductive additives.^{12b} Kung' group synthesized flexible

^aDepartment of Materials Science & Engineering, South University of Science and Technology of China, Shenzhen, Guangdong, China. E-mail: luzg@sustc.edu.cn; Fax: +86 88018904; Tel: +86 88018966

^bDepartment of Physics and Materials Science, City University of Hong Kong, 83 Tat Chee Avenue, Kowloon, Hong Kong, China

FeF₃-graphene composite paper by combining co-assembly and photothermal reduction, demonstrating that a conducting network of graphene sheets resulted in a high charge storage capacity, good rate and cycling performance.¹³ FeF₃·0.33H₂O/graphene was fabricated by Li *et al.* via an ionic-liquid-assisted synthetic approach, delivering a superior rate capability with a high specific capacity of 115 mA h g⁻¹ after 250 cycles at a large current density of 8 A g⁻¹.¹⁴ Despite the significant improvements achieved, the cost-effectiveness and mass production of the fabrication method and the further improvement of electrochemical performance are still not satisfactory.

Herein, we report a productive fabrication of FeF₃/C nanocomposites in a tailored autoclave via a novel vapour-solid (VS) method. The FeF₃ nanocrystals dispersed in a porous carbon matrix were transformed from Fe/Fe₂O₃/C nanocomposites through treatment by HF solution vapour at an elevated temperature. The phase evolution in the reaction process was investigated by XRD and the formation mechanism was discussed. Compared with bare FeF₃, the as-fabricated FeF₃/C composite shows an improved rate capability and cycling stability when used as the cathode material for LIBs, which can be attributed to the contribution from the porous carbon matrix which serves as a connected conductive medium for insulated FeF₃ particles.

2. Experimental section

Preparation of the precursor-Fe/Fe₂O₃/C nanocomposites

Fe/Fe₂O₃/C nanocomposites were fabricated by utilizing an ion exchange resin (styrene, macroporous) D001 as a precursor, as referred to in our recent work.¹⁵ The polystyrene-based cation-exchange resins (D001) were first soaked with absolute ethanol for 10 h to remove adsorbed organic components, treated with 5% HCl solution and then washed with deionized water until the eluate had a neutral pH. Subsequently, the wet resins were dried under vacuum at 60 °C for 12 h. After soaking in 0.1 mol L⁻¹ Fe(NO₃)₃ solution for 6 h, 1 g of resins above was washed with deionized water and dried under vacuum. Then the Fe-containing D001 resins were placed into a ceramic boat and heated from room temperature (RT) to 800 °C, at which temperature they were stayed for 2 h in a tube furnace under N₂ flow (150 mL min⁻¹). After cooling, the product was washed, dried, ground and then sieved through a 80–140 mesh. The resulting carbon was identified as precursor-Fe/Fe₂O₃/C nanocomposites.

Preparation of FeF₃/C nanocomposites and bare FeF₃

0.3 g of the as-prepared Fe/Fe₂O₃/C nanocomposite was wrapped in filter paper. The wrapped powders were put in a Teflon cylinder, which was placed higher than the level of HF solution. Then, the cylinder with the wrapped powders was transferred into a 90 mL Teflon-lined autoclave with 30 mL HF solution (48 wt%) and sealed by a stainless-steel shell. For comparison, another sample was prepared in a glovebox filled with argon gas. The autoclave was moved to be heated after it had been tightly sealed. (Note the HF solution is highly corrosive and

must be handled with suitable precautions at all times; contact with the skin must be avoided). The reaction system was kept at 120 °C for 3 h (or other designated time). After naturally cooling to RT, the wrapped powders (FeF₃·3H₂O/C) were taken out, washed with ethanol and water several times, and dried at 60 °C for 10 h in a vacuum oven. The final product (FeF₃/C) was obtained after heat-treating FeF₃·3H₂O/C at 200 °C for 4 h under a continuous high-purity Ar gas flow. Bare FeF₃ was fabricated by the same procedure, except using Fe₃O₄ particles as a precursor. Fe₃O₄ particles were synthesized according to procedures given in the literature.¹⁶

Physical characterization

X-ray diffraction (XRD) patterns in the 2θ range of 15–85° were obtained by employing a Siemens D500 diffractometer with Cu Kα radiation at a scan rate of 0.02° s⁻¹. To confirm the content of graphene in the as-prepared FeF₃/C nanocomposites, thermogravimetric (TG, Q50) analysis was employed from RT to 700 °C under air ventilation of 40 mL min⁻¹ at a heating rate of 5 °C min⁻¹. The morphology of the precursor and FeF₃/C nanocomposites was examined with a Philips XL30 FEG field-emission scanning electron microscope (FESEM). Transmission electron microscopy (TEM) images were obtained by JEOL JEM 2100F microscope operated at 200 kV. The specific surface areas and pore size of the FeF₃/C and FeF₃ samples were analyzed by nitrogen (N₂) adsorption/desorption isotherms at 77 K using a NOVA 1200e Surface Area and Pore Size Analyzer (Quantachrome Instruments) within a pressure range of 0.05–0.99 P/P₀ (relative pressure). Prior to adsorption experiments, the samples were outgassed in vacuum at 150 °C for 2 h.

Electrochemical performance evaluation

The active material (FeF₃/C) and poly(vinylidene fluoride) (PVDF) binder with a mass ratio 4 : 1 were dispersed in a *N*-methylpyrrolidone (NMP) solution. No carbon black was added. The resultant slurry was then uniformly coated on an Al foil current collector and dried overnight under vacuum at 100 °C. For comparison, bare FeF₃, carbon black (the amount equals the weight percentage of porous carbon in the FeF₃/C) and PVDF were dispersed in NMP. The mass ratio of the sum of FeF₃ and carbon black to PVDF binder was also 4 : 1. After drying in a vacuum oven, the Al foil with the active material was punched into circular discs (1.6 cm²). Coin cells (CR2032) were assembled with lithium metal foil as the counter-electrode, Celgard 2400 membrane acted as the separator and LiPF₆ (1 M) in ethylene carbonate/dimethyl carbonate (EC/DMC, 1 : 1 vol%) was the electrolyte. Both cyclic voltammograms (CV) and impedance measurements were performed on a Zahner IM6 electrochemical workstation. CV curves were recorded at RT between 1.5 and 4.5 V (vs. Li⁺/Li) at a scan rate of 0.2 mV s⁻¹. Galvanostatic electrochemical experiments were carried out (Arbin Instruments, College Station, TX) between 1.5 and 4.5 V vs. Li⁺/Li at RT, at different current densities for rate performance and at 20.8 mA g⁻¹ for cycling performance. Electrochemical impedance spectra (EIS) were obtained after a 2 h rest by applying an AC voltage of 2.5 mV amplitude over the

frequency range from 100 kHz to 10 mHz after 50 cycles. The EIS parameters were simulated by ZSIMPWIN software.

3. Results and discussion

Fig. 1a shows the XRD pattern of Fe/Fe₂O₃/C. All the diffraction peaks are assigned to Fe₂O₃ (JCPDS no. 39-1346) and Fe (JCPDS no. 06-0669), while the broad hump centred at 26.6° is ascribed to the carbon matrix. The Fe/Fe₂O₃/C nanocomposites powder was heat treated with 48% HF solution vapour at 120 °C for different reaction times (e.g. 1 h, 2 h, and 3 h) in a sealed home-made autoclave.¹⁷ As shown in Fig. 1b, it was observed that two sets of peaks attributed to the Fe₂O₃ (JCPDS no. 40-1139 and JCPDS no. 33-0664, marked by black dots and red squares, respectively) appeared when the VS reaction lasted for 1 h. One peak at 46.9°, marked by inverted triangle, cannot be accurately indexed indicating the existence of an intermediate, but the phase is uncertain due to there being only one peak. With the increase of reaction time, (e.g. 2 h), the intensity of all the intermediate peaks decreased, whereas the peaks assigned to FeF₃·3H₂O (JCPDS no. 33-0664) became obvious and their intensity increased. When the reaction time reached up to 3 h, the phases of intermediates disappeared and FeF₃·3H₂O formed completely. After annealing FeF₃·3H₂O/C at 200 °C for 4 h, FeF₃/C was obtained, as shown in Fig. 1c.

The XRD results of the reaction process were consistent with the thermodynamic simulation. The Gibbs energy change for each reaction at 1.0 bar pressure was calculated by utilizing the software (Mathcad 2001i Professional) as a function of temperature, as presented in Fig. 2. It was noted that the energy change of reaction between Fe and oxygen was much larger than that of reaction between Fe and HF. For example, at 120 °C

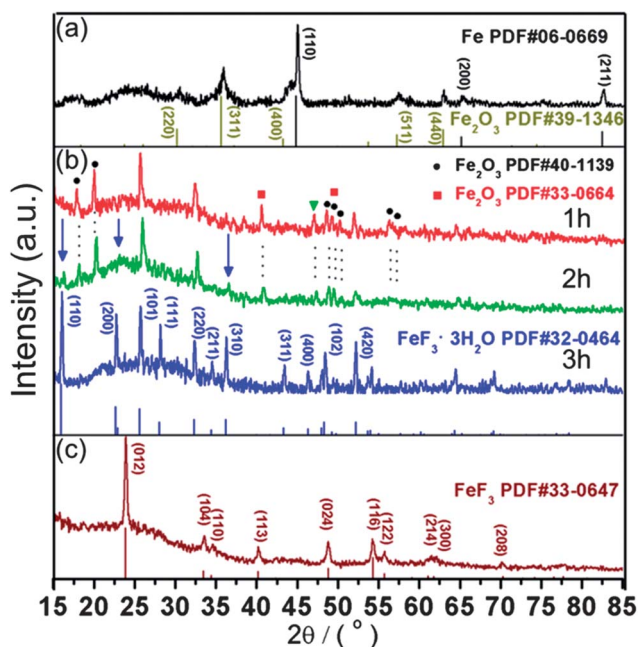


Fig. 1 XRD patterns of the precursor (Fe/Fe₂O₃/C), intermediates and FeF₃/C produced in an autoclave full of air.

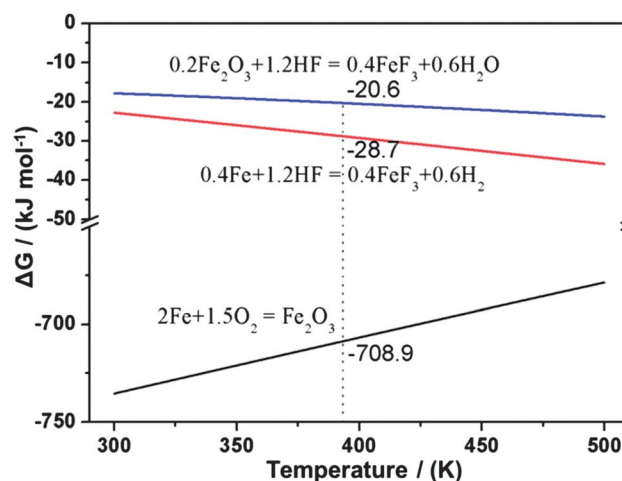


Fig. 2 Gibbs energy changes of the reactions between Fe and oxygen, between Fe and HF, and between Fe₂O₃ and HF, respectively.

(393.15 K), the Gibbs energy change for the reaction between Fe and O₂ is about $-708.9 \text{ kJ mol}^{-1}$, almost 25 times the value for the reaction between Fe and HF. This means that the Fe nanoparticles preferentially oxidize to Fe₂O₃ rather than directly fluoridizing to FeF₃. The resultant Fe₂O₃ reacted with HF solution vapour to form FeF₃·3H₂O.

To prove the role of air in forming the FeF₃, we filled the autoclave with argon gas by placing the autoclave in a glovebox filled with Ar gas. The autoclave was then heat treated at 120 °C for different reaction times. Fig. 3a shows the XRD result of the product reacted for 3 h, revealing that the phase became amorphous. A trace of Fe₂O₃ still remained in the powder, as marked by the red dots, indicating that the reaction was not completely finished. For comparison, the pattern of precursor, Fe/Fe₂O₃/C, is also shown. When the reaction time was prolonged to 6 h, the product was still amorphous, as shown in

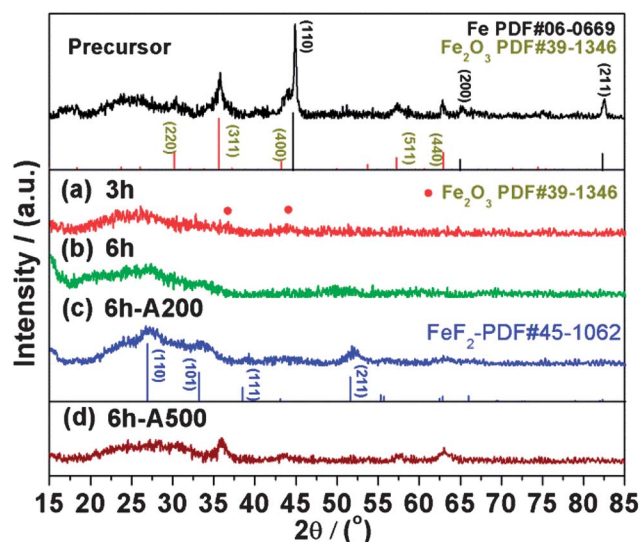


Fig. 3 XRD patterns of the intermediates and final product produced in the autoclave filled with Ar gas.

Fig. 3b. To confirm the phase of the product, the powder was annealed at 200 °C and 500 °C (denoted as “6h-A200” and “6h-A500”), respectively, in an argon atmosphere. After annealing at 200 °C for 4 h, the powder became FeF_2 (JCPDS no. 45-1062) labelled as “6h-A200” in Fig. 3c. The powder annealed at 500 °C (denoted as “6h-A500” in Fig. 3d) was completely converted to Fe_2O_3 (JCPDS no. 39-1346), indicating that the powder before annealing contained an oxygen element.

Based on the previous studies,^{18,19} we speculated that as the HF solution containing 52 wt% water, the hydrated H_2O molecules played significant role in the formation of the amorphous intermediates in the process of heat treatment. So the amorphous powder could be formalised as $\text{FeF}_x \cdot y\text{H}_2\text{O}$ ($x < 3$). Based on the results of Fig. 1–3, we summarized the phase evolution of the reaction between the precursor and HF solution vapour, as shown in Fig. 4. Different reaction atmospheres result in distinct products. It is worth pointing out that the air in the autoclave plays an important role in driving the reaction between the precursor and the HF solution vapour, and the resultant crystallization.

Fig. 5a and b show the SEM and TEM images of $\text{Fe}/\text{Fe}_2\text{O}_3/\text{C}$ nanocomposite, respectively. SEM image (Fig. 5a) does not display any unique structure of $\text{Fe}/\text{Fe}_2\text{O}_3/\text{C}$, but the TEM image (Fig. 5b) reveals that some $\text{Fe}/\text{Fe}_2\text{O}_3$ particles ranging from 20 to 50 nm, together with some pores, were dispersed in the carbon matrix. The dark areas are the $\text{Fe}/\text{Fe}_2\text{O}_3$ particles, while the bright areas are pores. This morphology is similar to porous carbon produced by carbonizing Cr-adsorbed D001 resins.¹⁵ Fig. 5c shows the SEM image of FeF_3/C , revealing the morphology variation from the $\text{Fe}/\text{Fe}_2\text{O}_3/\text{C}$ to FeF_3/C . From the SEM image we observed only the FeF_3 particles formed on the surface of the carbon matrix, such as the cubes, rods both marked by white rectangles. TEM image (Fig. 5d) further displays that the cubic FeF_3 particles (FeF_3 rods), ranging in size from 150 to 400 nm, were dispersed into the porous carbon matrix. In the inset of Fig. 5d, the diffraction dots can be indexed to planes of (012) and (104) of FeF_3 , agreeing well with the XRD pattern in Fig. 1c, which indicates good crystallinity of FeF_3 . This unique structure is expected to improve the

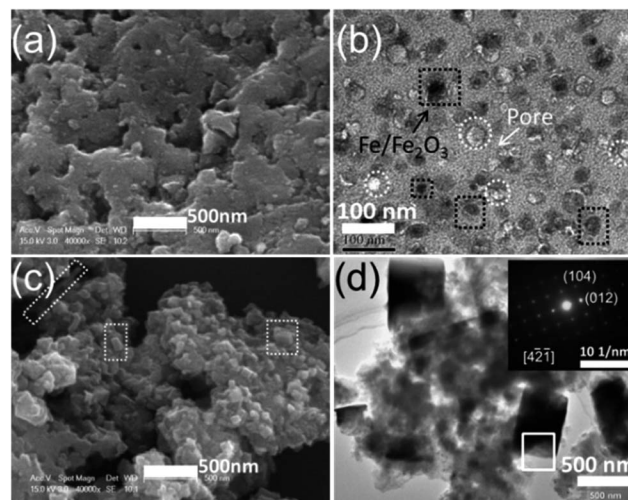


Fig. 5 (a) SEM and (b) TEM images of $\text{Fe}/\text{Fe}_2\text{O}_3/\text{C}$ nanocomposites; (c) SEM and (d) TEM images FeF_3/C composites; inset of (d) shows the SAED of the area indicated in white.

electrochemical performance of FeF_3 as a cathode material for LIBs from three aspects. Firstly, the carbon matrix can buffer the volume change during the discharge/charge process.^{20,21} Secondly, the porous structure of carbon matrix is favourable for the permeation of electrolyte, thus promoting the reaction kinetics of FeF_3 .^{22,23} Lastly, the carbon matrix can maintain the integrity of insulated FeF_3/LiF with electrical conductive carbon in the charge/discharge process.²⁴

The weight of $\text{FeF}_3 \cdot 3\text{H}_2\text{O}/\text{C}$ was quantitatively determined by thermogravimetric (TG) analysis in air, as shown in Fig. 6. The small weight loss below 120 °C is likely to be due to the evaporation of moisture or gaseous content in the powder. As the temperature increases, the weight decreases distinctly from 120 °C to 500 °C, resulting from the combustion of carbon. The change trend of weight agrees well with that shown in the literature.¹⁸ The final product of heat treating $\text{FeF}_3 \cdot 3\text{H}_2\text{O}$ above 500 °C was Fe_2O_3 . Based on the TG curve and the final residue (Fe_2O_3), the weight percentage of

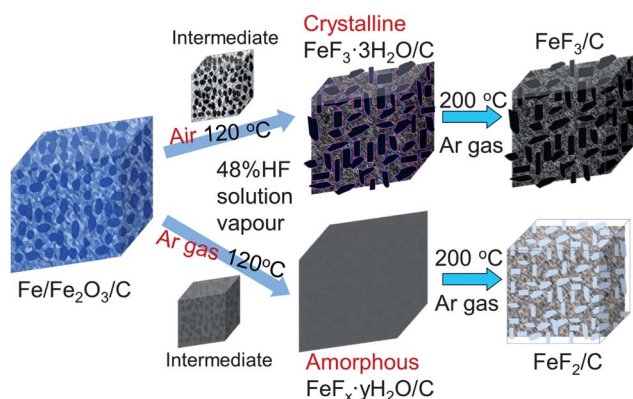


Fig. 4 Scheme of phase evolution upon the reaction between the precursor and HF solution vapour under different atmospheres.

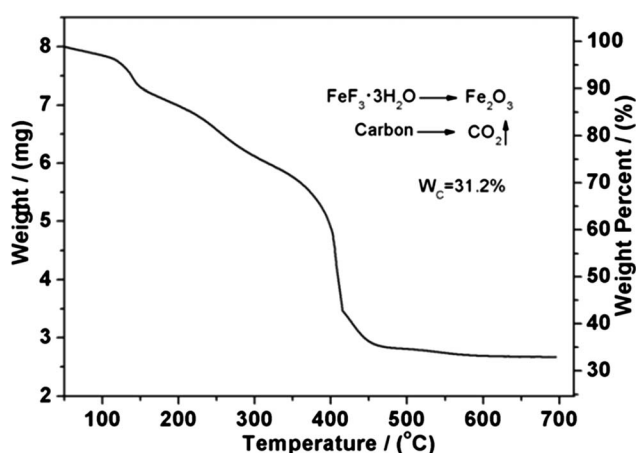


Fig. 6 TG curve of $\text{FeF}_3 \cdot 3\text{H}_2\text{O}/\text{C}$ from room temperature to 700 °C in air.

$\text{FeF}_3 \cdot 3\text{H}_2\text{O}$ in the sample was estimated to be $\sim 68.81\%$. After annealing at 200°C for 4 h, $\text{FeF}_3 \cdot 3\text{H}_2\text{O}/\text{C}$ became FeF_3/C , so the weight percent of FeF_3 in the FeF_3/C was calculated to be $\sim 59.87\%$.

Electrochemical performance of FeF_3/C was evaluated as a cathode material for LIBs by assembling a coin cell (CR2032). Due to the relatively high carbon content ($\sim 40.13\%$) in the FeF_3/C nanocomposites, there is no conductive agent (carbon black) added to the slurry when preparing the electrode disc. For comparison, bare FeF_3 fabricated by a VS method was also tested as a cathode for LIBs, by mixing with the same amount ($\sim 40.13\%$) of carbon black. Fig. 7a shows typical cyclic voltammograms of FeF_3/C recorded at 0.2 mV s^{-1} between 1.5 and 4.5 V. In the cathodic process of the first cycle, a broad reduction peak located at about 2.5 V is observed. In the subsequent cycles the broad peak shifts to $\sim 2.92\text{ V}$ and a tiny cathodic peak appears at 3.26 V, which should correspond to the intercalation reaction (eqn (1)) and conversion reaction (eqn (2)), respectively.^{5,9,25}



During the anodic process of the first cycle, it is clear that there are two oxidation peaks approximately located at 2.81 and 3.41 V, corresponding to the inverse reactions of eqn (1) and (2), respectively. In the subsequent cycles, the voltage

difference of these two reduction peaks becomes smaller, which means the average voltage hysteresis decreases roughly from 0.60 V in the first cycle to 0.49 V in the subsequent cycles. This is because the phase separation and recombination becomes easier, as a result of pulverization of the FeF_3 particles in the first cycle.^{26,27} Thereby, the transport of Li ions and electrons is promoted due to the decrease in size.

Fig. 7b illustrates the respective rate capability of FeF_3/C and bare FeF_3 at different current densities. The inset of Fig. 7b shows the TEM image of bare FeF_3 , revealing that FeF_3 particles with a size from 100 to 200 nm form aggregates. All the cells were firstly activated at 10.4 mA g^{-1} for 2 cycles, unless otherwise specified. The cells used for testing rate capability were then cycled at 20.8, 104, 520, and 1040 mA g^{-1} for 5 cycles, respectively. The FeF_3/C presents the discharge capacity of 246.3, 134.3, 103.2 and 71.0 mA h g^{-1} in sequence, whereas the FeF_3 only delivers 241.2, 109.3, 84.1 and 43.0 mA h g^{-1} . The rate performance of FeF_3/C is superior to that of FeF_3 , which is likely to be caused by the good integrity of carbon and FeF_3/LiF particles during the cycling process. However, due to the nature of the conversion reaction, the advantage of rate capability is not very remarkable. Fig. 7c presents the stable cyclability of FeF_3/C over 50 cycles at 20.8 mA g^{-1} . It can be seen that after 50 cycles, the discharge and charge capacities of FeF_3/C at 20.8 mA g^{-1} still remained 198.9 and 196.3 mA h g^{-1} , with a Coulombic efficiency of 98.7%, showing better stability than FeF_3 , which only remained at 104.0 and 103.7 mA h g^{-1} after 50 cycles, with a Coulombic efficiency of 99.7%. The inset shows

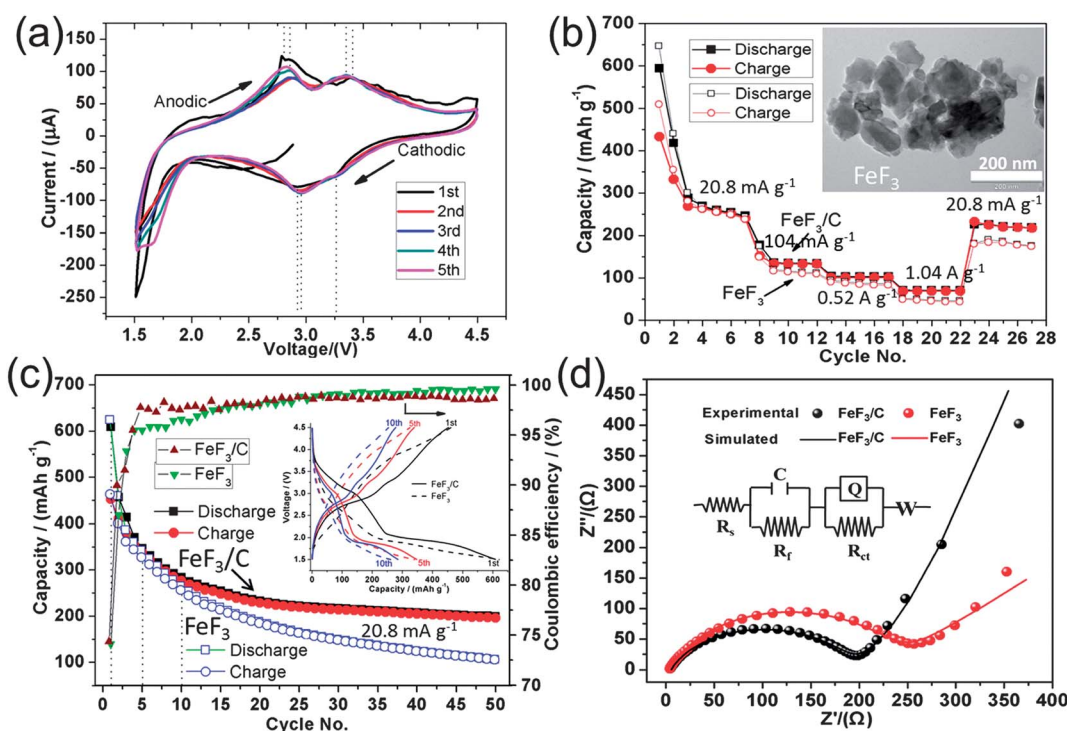


Fig. 7 (a) Cyclic voltammograms of FeF_3/C nanocomposites; (b) rate capability of FeF_3/C and FeF_3 , respectively; the inset shows the TEM image of bare FeF_3 ; (c) cycling performance, Coulombic efficiency and (inset) voltage profiles of the 1st 5th and 10th cycle of FeF_3/C and bare FeF_3 respectively; (d) EIS of FeF_3/C and FeF_3 after 50 cycles and equivalent circuit used for simulation. Symbols represent experimental data and continuous lines represent a simulated curve.

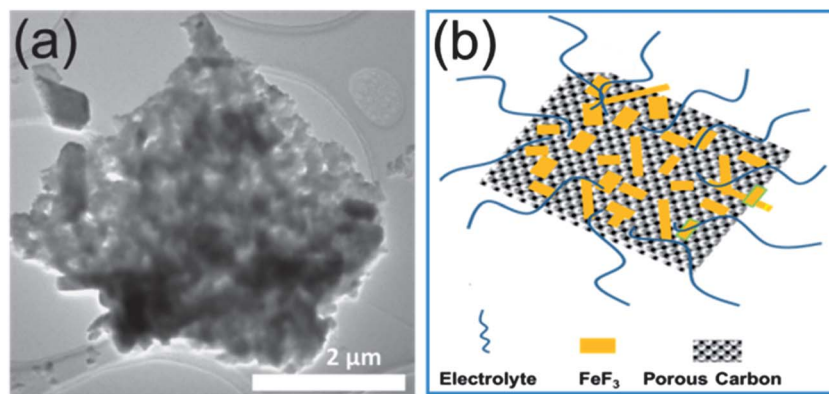


Fig. 8 (a) Low-magnification TEM image of FeF_3/C clearly reveals the porous structure of carbon matrix; (b) scheme of electrolyte penetration into the FeF_3/C .

voltage profiles of the 1st, 5th and 10th cycle of FeF_3/C and bare FeF_3 , respectively. We note that FeF_3/C and bare FeF_3 show comparable discharge/charge capacities (608.4 , $452.4 \text{ mA h g}^{-1}$ for FeF_3/C and 621.7 , $461.2 \text{ mA h g}^{-1}$ for FeF_3 , respectively) in the initial cycle, with an initial Coulombic efficiency of 74.4% and 74.2% , respectively. In the 5th cycle, the capacities of FeF_3/C and bare FeF_3 kept comparable but in the 10th cycle, the discharge and charge capacities of FeF_3/C were 284.1 and $277.1 \text{ mA h g}^{-1}$, while for FeF_3 were 262.8 and $254.0 \text{ mA h g}^{-1}$, respectively. We noted that the Coulombic efficiency of both FeF_3/C and FeF_3 gradually increases during the first ten cycles, indicative of the activation of electrode materials.²⁸ After the 10th cycle, the capacity difference becomes obvious. The capacity of FeF_3/C decreased by 0.69% per cycle, whereas the capacity of FeF_3 by 1.47% per cycle. The improved capacity and stability of FeF_3/C could be attributed to the buffering effect of the carbon matrix because the carbon matrix plays an important role in interconnecting the FeF_3 particles as well as accommodating the volume change during the electrochemical reaction.

Fig. 7d shows Nyquist plots of FeF_3/C and FeF_3 after 50 cycles, respectively. The data were analysed by fitting to an equivalent electrical circuit shown in the inset of Fig. 7d.²⁹ The equivalent circuit model includes Ohmic resistance (R_s) corresponding to Li^+ transport in electrolyte, a resistance (R_f) and a

capacitor (C) attributed to Li^+ migration through the multilayer surface films, a resistance (R_{ct}) and a constant phase element (CPE) related to the charge transfer through the electrode/electrolyte interface, and a Warburg impedance (W) associated with Li^+ diffusion in FeF_3 particles.^{30,31} The fitted EIS parameters are in good agreement with the experimental data. The charge-transfer resistance R_{ct} of FeF_3/C is $\sim 183.6 \Omega$, smaller than the value ($\sim 219.5 \Omega$) of FeF_3 . This is closely related to the improvement of electronic conductivity due to the combination of FeF_3 with carbon.³² This is definitely favourable for the transport of electrons and reaction of Li^+ ions with active material.³³

On one hand the improved electrochemical performance can be attributed to the intimate contact of FeF_3 particles within the porous carbon matrix, which improves the electronic conductivity. On the other hand, the high specific surface area and the porous structure of carbon matrix also contribute largely to the diffusion kinetics by promoting the permeation of electrolyte. As shown in Fig. 8a, low-magnification TEM image of FeF_3/C clearly shows the porous structure of the carbon matrix on a large scale, $\sim 5 \mu\text{m}$, displaying pore sizes ranging from 50 to 100 nm . The porous structure of the carbon matrix and high specific surface area increased the contact area of the active material with electrolyte, which is beneficial for electrolyte

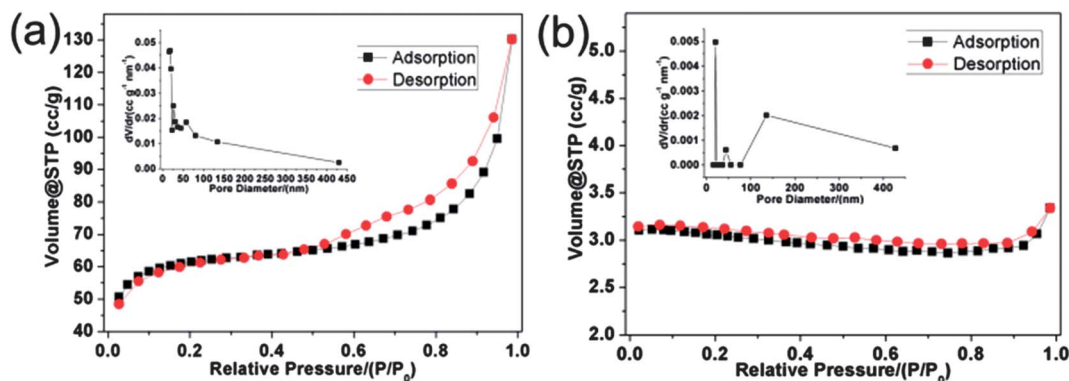


Fig. 9 N_2 sorption isotherms of (a) FeF_3/C and (b) FeF_3 powder, respectively. The insets show the corresponding pore size distribution curves.

infiltration and Li^+ ions diffusion, as depicted in Fig. 8b, thereby improving the transport kinetics. This is another reason why the FeF_3 dispersed into porous carbon matrix possesses superior electrochemical performance to bare FeF_3 , as well as the increased electrical conductivity by carbon.

The Brunauer–Emmett–Teller (BET) measurement further confirms the porous structure of the carbon matrix. As shown in Fig. 9, a type IV isotherm with a type H1 hysteresis loop and a typical capillary condensation step was observed for the FeF_3/C sample, which is characteristic of a porous architecture with a wide range pore size distribution ranging from a few nanometers to hundreds of nanometers. The pore size calculated from the desorption branch of the isotherm by the BJH (Barrett–Joyner–Halenda) method is located at ~ 57 nm, corresponding to a mesoporous size range (inset of Fig. 9a). In contrast, the N_2 adsorption–desorption isotherm of FeF_3 sample presents type II-like curve, as shown in Fig. 9b, indicating the features of no pores or macropores. The pore size derived from the desorption isotherm (inset of Fig. 9b) is higher than 150 nm, which is consistent with the observation of TEM (inset of Fig. 7b). The specific surface area of the FeF_3/C sample and FeF_3 sample is ~ 204.7 and $6.9 \text{ m}^2 \text{ g}^{-1}$, respectively. This suggests that the specific surface area is considerably increased due to the existence of the porous carbon matrix.

4. Conclusions

In summary, FeF_3/C nanocomposites, where FeF_3 nanocrystals were well dispersed within a porous carbon matrix, have been successfully fabricated by a novel vapour–solid method in a tailored autoclave. Phase transition investigation shows that the air in the autoclave plays an important role in driving the reaction to finally form FeF_3 . The as-prepared FeF_3/C delivers 134.3, 103.2 and 71.0 mA h g^{-1} of charge capacity at a current density of 104, 520, and 1040 mA g^{-1} in turn, exhibiting superior rate capability to the bare FeF_3 . Moreover, it displays more stable cycling performance, with a charge capacity of $196.3 \text{ mA h g}^{-1}$ at 20.8 mA g^{-1} . The good electrochemical performance can be attributed to the buffering effect, good electrical conductivity and high specific surface area, resulting from the porous carbon matrix.

Acknowledgements

This work is supported by the National Natural Science Foundation of China (21001117) and the Starting Up Funds of South University of Science and Technology of China (SUSTC).

References

- 1 J. B. Goodenough and K. S. Park, *J. Am. Chem. Soc.*, 2013, **135**(4), 1167–1176.
- 2 C. Li, L. Gu, J. Tong and J. Maier, *ACS Nano*, 2011, **5**(4), 2930–2938.
- 3 C. Li, L. Gu, J. Tong, S. Tsukimoto and J. Maier, *Adv. Funct. Mater.*, 2011, **21**(8), 1391–1397.
- 4 C. Li, C. Yin, X. Mu and J. Maier, *Chem. Mater.*, 2013, **25**(6), 962–969.
- 5 F. Wang, R. Robert, N. A. Chernova, N. Pereira, F. Omenya, F. Badway, X. Hua, M. Ruotolo, R. Zhang, L. Wu, V. Volkov, D. Su, B. Key, M. S. Whittingham, C. P. Grey, G. G. Amatucci, Y. Zhu and J. Graetz, *J. Am. Chem. Soc.*, 2011, **133**(46), 18828–18836.
- 6 M. Armand and J. M. Tarascon, *Nature*, 2008, **451**(7179), 652–657.
- 7 P. G. Bruce, S. A. Freunberger, L. J. Hardwick and J. M. Tarascon, *Nat. Mater.*, 2012, **11**(1), 19–29.
- 8 (a) G. G. Amatucci and N. Pereira, *J. Fluorine Chem.*, 2007, **128**(4), 243–262; (b) T. Li, L. Li, Y. L. Cao, X. P. Ai and H. X. Yang, *J. Phys. Chem. C*, 2010, **114**(7), 3190–3195.
- 9 F. Badway, F. Cosandey, N. Pereira and G. G. Amatucci, *J. Electrochem. Soc.*, 2003, **150**(10), A1318–A1327.
- 10 F. Badway, N. Pereira, F. Cosandey and G. G. Amatucci, *J. Electrochem. Soc.*, 2003, **150**(9), A1209–A1218.
- 11 W. Wu, X. Wang, X. Wang, S. Yang, X. Liu and Q. Chen, *Mater. Lett.*, 2009, **63**(21), 1788–1790.
- 12 (a) S. W. Kim, D. H. Seo, H. Gwon, J. Kim and K. Kang, *Adv. Mater.*, 2010, **22**(46), 5260–5264; (b) W. Zhang, L. Ma, H. Yue and Y. Yang, *J. Mater. Chem.*, 2012, **22**(47), 24769–24775.
- 13 X. Zhao, C. M. Hayner, M. C. Kung and H. H. Kung, *Chem. Commun.*, 2012, **48**(79), 9909–9911.
- 14 B. Li, D. W. Rooney, N. Zhang and K. Sun, *ACS Appl. Mater. Interfaces*, 2013, **5**(11), 5057–5063.
- 15 J. Hu, P. P. Tao, S. Wang, Y. Liu, Y. G. Tang, H. Zhong and Z. G. Lu, *J. Mater. Chem. A*, 2013, **1**(22), 6558–6562.
- 16 K. F. Zhou, Y. H. Zhu, X. L. Yang and C. Z. Li, *New J. Chem.*, 2010, **34**(12), 2950–2955.
- 17 R. G. Ma, Z. G. Lu, C. D. Wang, H. E. Wang, S. Yang, L. J. Xi and C. Y. Chung, *Nanoscale*, 2013, **5**, 6338–6343.
- 18 R. G. Ma, L. F. He, Z. G. Lu, S. L. Yang, L. J. Xi and C. Y. Chung, *CrystEngComm*, 2012, **14**(23), 7882–7887.
- 19 L. Li, Y. Yu, F. Meng, Y. Tan, R. J. Hamers and S. Jin, *Nano Lett.*, 2012, **12**(2), 724–731.
- 20 D. L. Ma, Z. Y. Cao, H. G. Wang, X. L. Huang, L. M. Wang and X. B. Zhang, *Energy Environ. Sci.*, 2012, **5**(9), 8538–8542.
- 21 R. G. Ma, Z. G. Lu, S. L. Yang, L. J. Xi, C. D. Wang, H. E. Wang and C. Y. Chung, *J. Solid State Chem.*, 2012, **196**, 536–542.
- 22 B. Fang, M. S. Kim, J. H. Kim, S. Lim and J. S. Yu, *J. Mater. Chem.*, 2010, **20**(45), 10253–10259.
- 23 T. Yoon, C. Chae, Y. K. Sun, X. Zhao, H. H. Kung and J. K. Lee, *J. Mater. Chem.*, 2011, **21**(43), 17325–17330.
- 24 F. Badway, A. N. Mansour, N. Pereira, J. F. Al-Sharab, F. Cosandey, I. Plitz and G. G. Amatucci, *Chem. Mater.*, 2007, **19**(17), 4129–4141.
- 25 Y. Ma and S. H. Garofalini, *J. Am. Chem. Soc.*, 2012, **134**(19), 8205–8211.
- 26 D. Larcher, C. Masquelier, D. Bonnin, Y. Chabre, V. Masson, J. B. Leriche and J. M. Tarascon, *J. Electrochem. Soc.*, 2003, **150**(1), A133–A139.
- 27 P. Liu, J. J. Vajo, J. S. Wan, W. Li and J. Liu, *J. Phys. Chem. C*, 2012, **116**(10), 6467–6473.

- 28 R. G. Ma, Y. C. Dong, L. J. Xi, S. L. Yang, Z. G. Lu and C. Y. Chung, *ACS Appl. Mater. Interfaces*, 2013, **5**(3), 892–897.
- 29 M. V. Reddy, T. Yu, C. H. Sow, Z. X. Shen, C. T. Lim, G. V. S. Rao and B. V. R. Chowdari, *Adv. Funct. Mater.*, 2007, **17**(15), 2792–2799.
- 30 L. J. Xi, H. E. Wang, Z. G. Lu, S. L. Yang, R. G. Ma, J. Q. Deng and C. Y. Chung, *J. Power Sources*, 2012, **198**, 251–257.
- 31 Y. L. Shi, M. F. Shen, S. D. Xu, Q. C. Zhuang, L. Jiang and Y. H. Qiang, *Solid State Ionics*, 2012, **222–223**, 23–30.
- 32 Y. Zhang, W. C. Wang, P. H. Li, Y. B. Fu and X. H. Ma, *J. Power Sources*, 2012, **210**, 47–53.
- 33 J. L. Yang, J. J. Wang, D. N. Wang, X. F. Li, D. S. Geng, G. X. Liang, M. Gauthier, R. Y. Li and X. L. Sun, *J. Power Sources*, 2012, **208**, 340–344.